

Pinning, Rotation, and Metastability of BiFeO₃ Cycloidal Domains in a Magnetic Field *

Randy S. Fishman

Materials Science and Technology Division, Oak Ridge National Laboratory, Oak Ridge, Tennessee 37831, USA

(Dated: November 6, 2021)

Earlier models for the room-temperature multiferroic BiFeO₃ implicitly assumed that a very strong anisotropy restricts the domain wavevectors \mathbf{q} to the three-fold symmetric axis normal to the static polarization \mathbf{P} . However, recent measurements demonstrate that the domain wavevectors rotate so that \mathbf{q} rotates within the hexagonal plane normal to \mathbf{P} away from the field orientation \mathbf{m} . We show that the previously neglected three-fold anisotropy K_3 restricts the wavevectors to lie along the three-fold axis in zero field. For \mathbf{m} along a three-fold axis, the domain with \mathbf{q} parallel to \mathbf{m} remains metastable below $B_{c1} \approx 7$ T. Due to the pinning of domains by non-magnetic impurities, the wavevectors of the other two domains start to rotate away from \mathbf{m} above 5.6 T, when the component of the torque $\boldsymbol{\tau} = \mathbf{M} \times \mathbf{B}$ along \mathbf{P} exceeds a threshold value τ_{pin} . Since $\boldsymbol{\tau} = 0$ when $\mathbf{m} \perp \mathbf{q}$, the wavevectors of those domains never become completely perpendicular to the magnetic field. Our results explain recent measurements of the critical field as a function of field orientation, small-angle neutron scattering measurements of the wavevectors, as well as spectroscopic measurements with \mathbf{m} along a three-fold axis.

PACS numbers: 75.25.-j, 75.30.Ds, 78.30.-j, 75.50.Ee

I. INTRODUCTION

The manipulation of magnetic domains with electric and magnetic fields is one of the central themes [1–3] in the study of multiferroic materials. Applications of multiferroic materials depend on a detailed understanding of how domains respond to external probes. Despite recent advances [4] in our understanding of the room-temperature multiferroic BiFeO₃, however, some crucial questions remain about how its cycloidal domains respond to a magnetic field.

A type I or “proper” multiferroic, BiFeO₃ exhibits a strong ferroelectric polarization of about 80 $\mu\text{C}/\text{cm}^2$ along one of the pseudo-cubic diagonals below the ferroelectric transition at $T_{FE} = 1100$ K [5,6]. Below T_{FE} , broken symmetry produces two Dzialoshinskii-Moriya (DM) interactions between the $S = 5/2$ Fe³⁺ ions. A magnetic transition at $T_N = 640$ K [7] allows the cycloidal spin state to take advantage of this broken symmetry.

Until recently, it seemed that a complete theoretical description [8–13] of rhombohedral BiFeO₃ was in hand. Employing the first available single crystals, the measured cycloidal frequencies [14–16] of BiFeO₃ provided a

stringent test for theory. A microscopic model for BiFeO₃ that includes two DM interactions D_1 and D_2 and single-ion anisotropy K_1 successfully predicted [12,13] the mode frequencies in zero field [14,15] and their magnetic field evolution [16] for several field orientations. Since all model parameters were determined [17] from the zero-field behavior of BiFeO₃, the field evolution of the cycloidal modes [13] provided a particularly good test of the microscopic model. Nevertheless, new evidence suggests that this model is not complete.

With the electric polarization $\mathbf{P} = P\mathbf{z}'$ along the pseudo-cubic diagonal $[1, 1, 1]$ ($[a, b, c]$ is a unit vector), the three magnetic domains of BiFeO₃ in zero field [18] have wavevectors $\mathbf{Q}_k = \mathbf{Q}_0 + \mathbf{q}_k$ where $\mathbf{Q}_0 = (\pi/a)(1, 1, 1)$ is the antiferromagnetic (AF) Bragg vector,

$$\mathbf{q}_1 = \frac{2\pi\delta}{a}(-1, 1, 0), \quad (1)$$

$$\mathbf{q}_2 = \frac{2\pi\delta}{a}(1, 0, -1), \quad (2)$$

$$\mathbf{q}_3 = \frac{2\pi\delta}{a}(0, -1, 1), \quad (3)$$

$a = 3.96$ Å is the lattice constant of the pseudo-cubic unit cell, and $\delta \approx 0.0045$ determines the cycloidal wavelength $\lambda = a/\sqrt{2}\delta \approx 620$ Å. In zero field, the three domains of BiFeO₃ with wavevectors \mathbf{q}_k are degenerate. For each domain k , the spins of the cycloid lie primarily in the plane defined by $\mathbf{z}' = [1, 1, 1]$ and \mathbf{x}' , which is the unit vector along \mathbf{q}_k . A magnetic field favors domains with $\mathbf{x}' \perp \mathbf{B}$ because $\chi_{\perp} \gg \chi_{\parallel}$ [19] for BiFeO₃.

The model described above successfully predicted the field dependence of the mode frequencies [13,16] when the stable domain has wavevector $\mathbf{q} \equiv \mathbf{Q} - \mathbf{Q}_0$ perpendicular to the magnetic field $\mathbf{B} = B\mathbf{m}$. For example, the mode frequencies with $\mathbf{m} = [0, 0, 1]$ and domain 1 or

*Copyright notice: This manuscript has been authored by UT-Battelle, LLC under Contract No. DE-AC05-00OR22725 with the U.S. Department of Energy. The United States Government retains and the publisher, by accepting the article for publication, acknowledges that the United States Government retains a non-exclusive, paid-up, irrevocable, world-wide license to publish or reproduce the published form of this manuscript, or allow others to do so, for United States Government purposes. The Department of Energy will provide public access to these results of federally sponsored research in accordance with the DOE Public Access Plan (<http://energy.gov/downloads/doe-public-access-plan>).

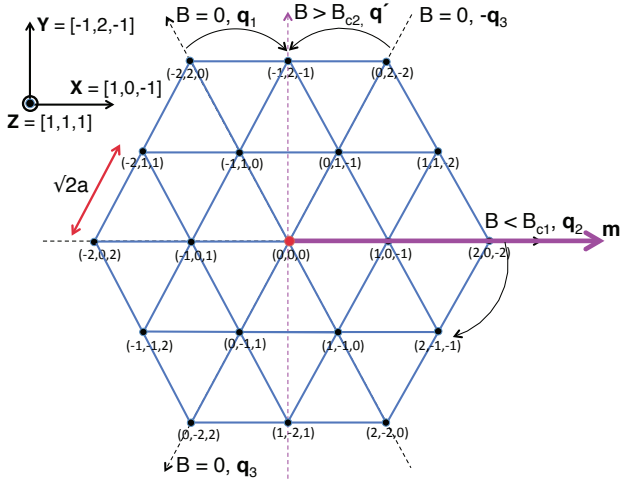


FIG. 1: (Color online) A hexagonal plane normal to \mathbf{Z} with $\mathbf{m} = \mathbf{X}$. In zero field, three domains with wavevectors \mathbf{q}_k are stable. Wavevectors \mathbf{q}_1 and \mathbf{q}_3 rotate towards $\mathbf{Y} \perp \mathbf{m}$ with increasing field. A domain with wavevector $\mathbf{q}' \parallel \mathbf{Y}$ is stable above B_{c2} in the absence of pinning. Below B_{c1} , the domain with wavevector \mathbf{q}_2 is metastable.

with $\mathbf{m} = [0, 1, 1]$ and domain 3 almost exactly match the theoretical predictions. But for \mathbf{m} along a three-fold symmetric axis like $[1, 0, -1]$, the mode frequencies are not as well described by taking the domain wavevector \mathbf{q} along $[-1, 1, 0]$ or $[0, -1, 1]$. Rather, the mode frequencies are then virtually identical to those with $\mathbf{m} = [-1, 2, -1]$ and \mathbf{q} along $[1, 0, -1] \perp \mathbf{m}$ [20]. In addition, the selection rules for the appearance of the spectroscopic modes do not follow the expected rules when the domain wavevectors lie along the three-fold axis [21]. So it appears that for a magnetic field along $\mathbf{m} = [1, 0, -1]$, the domain wavevectors \mathbf{q}_1 and \mathbf{q}_3 rotate away from \mathbf{m} towards $[-1, 2, -1]$, as indicated in Fig.1.

Another discrepancy appears in measurements of the critical field $B_{c3}(\mathbf{m})$ above which the canted AF (CAF) phase becomes stable. Predictions based on the “canonical” model indicate that $B_{c3}(\mathbf{m})$ depends on the stable domain as \mathbf{m} is rotated about $\mathbf{z}' = [1, 1, 1]$ by the azimuthal angle ζ [22]. However, experimental measurements [23,24] find that $B_{c3}(\mathbf{m})$ depends primarily on the polar angle $\vartheta = \cos^{-1}(\mathbf{m} \cdot \mathbf{z}')$ and does not sensitively depend on the azimuthal angle ζ .

Direct evidence for domain rotation in a magnetic field was recently provided by small angle neutron-scattering (SANS) [25]. Those measurements indicate that the metastable domain with wavevector \mathbf{q} along \mathbf{m} is slowly depopulated with increasing field and disappears above about 7 T. The other two domains start to merge into a single domain with wavevector perpendicular to \mathbf{m} but $\mathbf{q} \cdot \mathbf{m}$ never reaches zero.

This behavior is caused by the pinning of domains by non-magnetic impurities. In a ferromagnet [26,27], domain walls move when the component of \mathbf{B} along the domain magnetization \mathbf{M} exceeds the pinning field B_{pin} .

In the strong-pinning limit with \mathbf{m} along a three-fold axis, cyclodial wavevectors \mathbf{q} begin to rotate away from \mathbf{m} when the component of the torque $\boldsymbol{\tau} = \mathbf{M} \times \mathbf{B}$ along \mathbf{z}' exceeds a threshold value τ_{pin} . Since \mathbf{M} is induced by the component of \mathbf{B} perpendicular to the cyclodial plane containing \mathbf{q} , $\boldsymbol{\tau} = 0$ when $\mathbf{q} \perp \mathbf{m}$. Consequently, the wavevector \mathbf{q} never becomes completely perpendicular to the external field unless it lies along a three-fold axis perpendicular to \mathbf{m} .

This paper improves the “canonical” model of BiFeO_3 to address the discrepancies described above. Section II discuss the present “canonical” model for BiFeO_3 . In Section III, we present the higher-order anisotropy terms that break three-fold symmetry. The next two sections describe the consequences of this modified model in the absence of pinning. Section IV.A treats the case where \mathbf{m} lies along a three-fold axis so that the wavevectors of the stable domains rotate away from the other two three-fold axis with increasing field. Section IV.B treats the case where \mathbf{m} is perpendicular to a three-fold axis so that the wavevector of the stable domain does not rotate. Section V discusses the effects of pinning and provides an exact solution for domain rotation in the strong-pinning limit. We modify the conclusions of Section IV to include the effects of pinning in Section VI. Section VII contains a conclusion. The magnetoelastic coupling of BiFeO_3 is examined in the Appendix.

II. THE “CANONICAL” MODEL

The “canonical” model of BiFeO_3 has the Hamiltonian

$$\begin{aligned} \mathcal{H} = & -J_1 \sum_{\langle i,j \rangle} \mathbf{S}_i \cdot \mathbf{S}_j - J_2 \sum_{\langle i,j' \rangle} \mathbf{S}_i \cdot \mathbf{S}_j \\ & + D_1 \sum_{\langle i,j \rangle} (\mathbf{z}' \times \mathbf{e}_{i,j}/a) \cdot (\mathbf{S}_i \times \mathbf{S}_j) \\ & + D_2 \sum_{\langle i,j \rangle} (-1)^{h_i} \mathbf{z}' \cdot (\mathbf{S}_i \times \mathbf{S}_j) \\ & - K_1 \sum_i (\mathbf{z}' \cdot \mathbf{S}_i)^2 - 2\mu_B B \sum_i \mathbf{m} \cdot \mathbf{S}_i, \end{aligned} \quad (4)$$

where $\mathbf{e}_{i,j} = a\mathbf{x}$, $a\mathbf{y}$, or $a\mathbf{z}$ connects the spin \mathbf{S}_i on site \mathbf{R}_i with its nearest neighbor \mathbf{S}_j on site $\mathbf{R}_j = \mathbf{R}_i + \mathbf{e}_{i,j}$. The integer layer number h_i is defined by $\sqrt{3}\mathbf{R}_i \cdot \mathbf{z}'/a$. The first DM interaction D_1 determines the cyclodial wavelength λ ; the second DM interaction D_2 produces a small tilt $\tau \approx 0.3^\circ$ of the spins out of the $\mathbf{x}' - \mathbf{z}'$ plane [8,10].

The first DM term in \mathcal{H} ,

$$\mathcal{H}_{D_1} = D_1 \sum_{\langle i,j \rangle} (\mathbf{z}' \times \mathbf{e}_{i,j}/a) \cdot (\mathbf{S}_i \times \mathbf{S}_j), \quad (5)$$

does not depend on the choice of domain and \mathbf{q}_k . In earlier [4] versions of the “canonical” model, this term was restricted to a specific domain of the cyclodial. For

TABLE I: Reference frames of BiFeO₃

unit vectors	description and values
{ x , y , z }	pseudo-cubic unit vectors x = [1, 0, 0], y = [0, 1, 0], z = [0, 0, 1]
{ x' , y' , z' }	rotating reference frame of cycloid x' ∥ q , z' = [1, 1, 1], y' = z' × x'
{ X , Y , Z }	fixed reference frame of hexagonal plane X = [1, 0, -1], Y = [-1, 2, -1], Z = [1, 1, 1]

domain 2 with **q**₂ parallel to **x'** = [1, 0, -1] and **y'** = **z'** × **x'** = [-1, 2, -1], it was written

$$\mathcal{H}'_{D_1} = -\frac{D_1}{\sqrt{2}} \sum_{\mathbf{R}_j = \mathbf{R}_i + a(\mathbf{x} - \mathbf{z})} \mathbf{y}' \cdot (\mathbf{S}_i \times \mathbf{S}_j), \quad (6)$$

where **R**_{*i*} and **R**_{*j*} are next-nearest neighbors of the pseudo-cubic unit cell that lie on the same hexagonal layer *h*_{*i*}. Because the wavelength of the cycloid is so long, \mathcal{H}' has the same static and dynamical properties as \mathcal{H} provided that \mathcal{H} is applied to the domain specified by \mathcal{H}'_{D_1} .

Why replace \mathcal{H}' with \mathcal{H} ? Unlike \mathcal{H}' , \mathcal{H} can be used to study any domain with **q**_{*k*} along a three-fold axis. As shown below, \mathcal{H} also describes the general case where **q** differs from a three-fold axis. While \mathcal{H}'_{D_1} involves the sum over next-nearest neighbors, \mathcal{H}_{D_1} involves the sum over nearest neighbors, which should dominate the DM interaction. Finally, the general form of \mathcal{H}_{D_1} given above was obtained from first-principles calculations [28].

To construct the local reference frame of a cycloid with wavevector **q** = **Q** - **Q**₀, we take

$$\mathbf{q} = \frac{2\sqrt{2}\pi\delta}{a|\mathbf{n}|} (n_x, n_y, n_z) = \frac{2\pi}{\lambda} \mathbf{x}', \quad (7)$$

where *n*_{*i*} are integers with no common factors. Then the unit vector along **q** is **x'** = (*n*_{*x*}, *n*_{*y*}, *n*_{*z*})/|**n**| and **y'** = **z'** × **x'** = (*n*_{*z*} - *n*_{*y*}, *n*_{*x*} - *n*_{*z*}, *n*_{*y*} - *n*_{*x*})/(√3|**n**|). With the local reference frame of a cycloid defined by the unit vectors {**x'**, **y'**, **z'**}, the spin at site **R**_{*i*} = (*l*, *m*, *o*)*a* is indexed by the integer *r* = **n** · **R**_{*i*}/a = *n*_{*x*}*l* + *n*_{*y*}*m* + *n*_{*z*}*o*. Assuming that the spins **S**_{*r*}^(*j*) on alternate layers *j* = 1 or 2 are identical functions of *r*, then *r* ranges from 1 to *M* = |**n**|/√2δ = λ|**n**|/a in the magnetic unit cell.

It is straightforward to show that

$$\frac{1}{N} \mathcal{H}_{D_1} = \frac{D_1}{2\sqrt{3}M} \sum_{r=1}^M \left\{ \begin{aligned} & \mathbf{x} \cdot \left[\mathbf{S}_r^{(1)} \times (\mathbf{S}_{r+n_z}^{(2)} - \mathbf{S}_{r-n_z}^{(2)} - \mathbf{S}_{r+n_y}^{(2)} + \mathbf{S}_{r+n_y}^{(2)}) \right] \\ & + \mathbf{y} \cdot \left[\mathbf{S}_r^{(1)} \times (\mathbf{S}_{r+n_x}^{(2)} - \mathbf{S}_{r-n_x}^{(2)} - \mathbf{S}_{r+n_z}^{(2)} + \mathbf{S}_{r+n_z}^{(2)}) \right] \\ & + \mathbf{z} \cdot \left[\mathbf{S}_r^{(1)} \times (\mathbf{S}_{r+n_y}^{(2)} - \mathbf{S}_{r-n_y}^{(2)} - \mathbf{S}_{r+n_x}^{(2)} + \mathbf{S}_{r+n_x}^{(2)}) \right] \end{aligned} \right\}. \quad (8)$$

Since **S**_{*r+M*}^(*j*) = **S**_{*r*}^(*j*), the index *r* + *n*_{*α*} can be taken mod *M* to lie between 1 and *M*. Because λ/a = *M*/|**n**| ≫ 1,

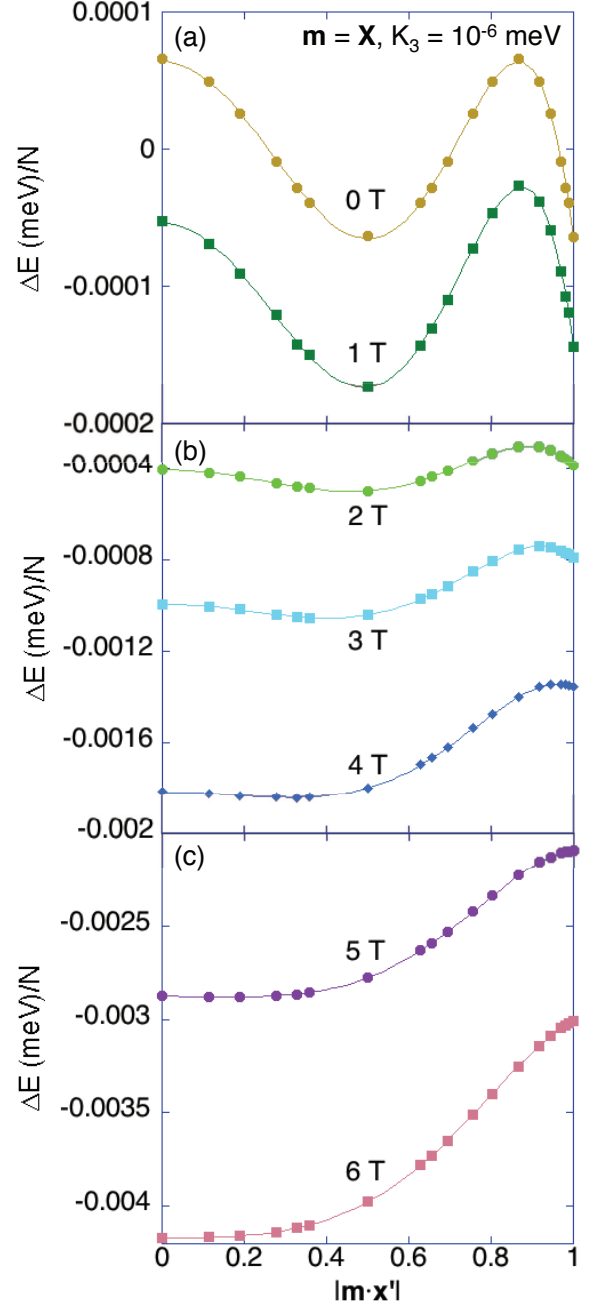


FIG. 2: (Color online) The energy $\Delta E/N$ versus wavevector $|\mathbf{m} \cdot \mathbf{x}'|$ for $K_3 = 10^{-6}$ meV and field ranging from 0 to 6 T along **X**. Solid curves are fits to a sixth order polynomial in $|\mathbf{m} \cdot \mathbf{x}'|$

$|n_i| \ll M$ and

$$\mathbf{S}_{r+n_i}^{(2)} - \mathbf{S}_{r-n_i}^{(2)} \approx n_i (\mathbf{S}_{r+1}^{(2)} - \mathbf{S}_{r-1}^{(2)}), \quad (9)$$

with corrections of order $\delta^3 \sim 10^{-7}$. This leads to the simpler form [29]

$$\frac{1}{N} \mathcal{H}_{D_1} = \frac{D_1 |\mathbf{n}|}{2M} \mathbf{y}' \cdot \sum_{r=1}^M \left\{ \mathbf{S}_r^{(1)} \times (\mathbf{S}_{r+1}^{(2)} - \mathbf{S}_{r-1}^{(2)}) \right\}. \quad (10)$$

Hence, the first DM interaction produces a cycloid in the $\mathbf{x}' - \mathbf{z}'$ plane for any wavevector $\mathbf{q} \parallel \mathbf{x}'$.

The second DM interaction, can be similarly written as [28]

$$\frac{1}{N} \mathcal{H}_{D_2} = \frac{3D_2}{M} \mathbf{z}' \cdot \sum_{r=1}^M (\mathbf{S}_r^{(1)} \times \mathbf{S}_r^{(2)}), \quad (11)$$

which rotates alternate layers of spins about the \mathbf{z}' axis and tilts the cycloid out of the $\mathbf{x}' - \mathbf{z}'$ plane

Neither of these DM interactions fixes the orientation of \mathbf{q} along a three-fold axis in zero field! To remedy that deficiency, we must add an additional term to the Hamiltonian that breaks the three-fold symmetry in the hexagonal plane perpendicular to \mathbf{z}' .

III. ANISOTROPY ENERGIES

Because $\{\mathbf{x}', \mathbf{y}', \mathbf{z}'\}$ already provides the reference frame for the cycloid, which can rotate in the plane perpendicular to \mathbf{z}' , we define $\mathbf{X} = [1, 0, -1]$ and $\mathbf{Y} = [-1, 2, -1]$ as fixed axis in the hexagonal plane. Of course, $\mathbf{Z} = \mathbf{X} \times \mathbf{Y} = [1, 1, 1]$ coincides with \mathbf{z}' and lies along \mathbf{P} . The three reference frames used in this paper are summarized in Table I.

The lowest-order anisotropy energy of BiFeO₃ was included in the ‘‘canonical’’ model:

$$\mathcal{H}_{K_1} = -K_1 \sum_i S_{iZ}^2. \quad (12)$$

The two next-order anisotropy terms consistent with the rhombohedral symmetry [30] of BiFeO₃ are

$$\begin{aligned} \mathcal{H}_{K_2} = & -\frac{1}{2} K_2 \sum_i S_{iZ} \\ & \times \left\{ (S_{iX} + iS_{iY})^3 + (S_{iX} - iS_{iY})^3 \right\}, \quad (13) \end{aligned}$$

$$\mathcal{H}_{K_3} = -\frac{1}{2} K_3 \sum_i \left\{ (S_{iX} + iS_{iY})^6 + (S_{iX} - iS_{iY})^6 \right\}. \quad (14)$$

Whereas K_1 is of order $l^2 |J_1|$ in terms of the dimensionless spin-orbit coupling constant l , K_2 and K_3 are of order $l^3 |J_1|$ and $l^4 |J_1|$, respectively [31]. These three terms have classical energies

$$E_{K_1} = \langle \mathcal{H}_{K_1} \rangle = -S^2 K_1 \sum_i \cos^2 \theta_i, \quad (15)$$

$$E_{K_2} = \langle \mathcal{H}_{K_2} \rangle = -S^4 K_2 \sum_i \cos \theta_i \sin^3 \theta_i \cos 3\phi_i, \quad (16)$$

$$E_{K_3} = \langle \mathcal{H}_{K_3} \rangle = -S^6 K_3 \sum_i \sin^6 \theta_i \cos 6\phi_i, \quad (17)$$

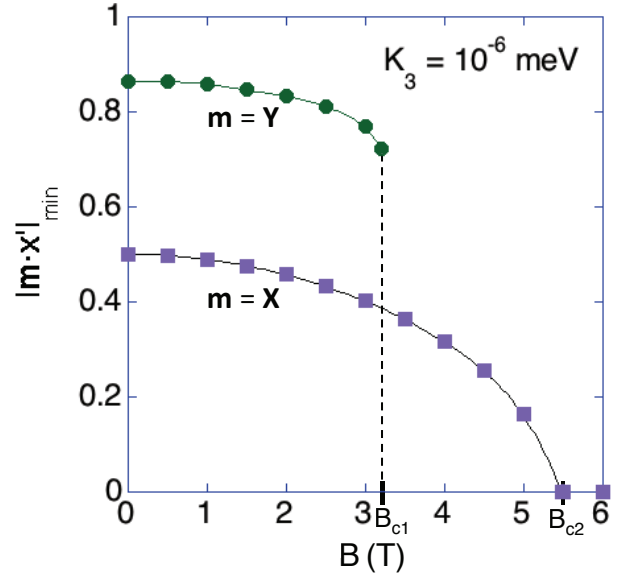


FIG. 3: (Color online) The wavevector $|\mathbf{m} \cdot \mathbf{x}'|_{\min}$ for stable ($\mathbf{m} = \mathbf{X}$, squares) and metastable ($\mathbf{m} = \mathbf{Y}$, circles) domains versus field with $K_3 = 10^{-6}$ meV.

where the spin

$$\langle \mathbf{S}_i \rangle = S \left\{ \cos \phi_i \sin \theta_i \mathbf{X} + \sin \phi_i \sin \theta_i \mathbf{Y} + \cos \theta_i \mathbf{Z} \right\} \quad (18)$$

is given in the fixed reference frame defined above. Other anisotropy energies $S^2 K_1' \sum_i \sin^2 \theta_i \cos 2\phi_i$ and $S^4 K_2' \sum_i \sin^4 \theta_i \cos 4\phi_i$ vanish for the $R3c$ crystal structure of BiFeO₃ [30,32].

For the distorted cycloid of the ‘‘canonical’’ model, both E_{K_1} and E_{K_3} are nonzero. Because the cycloid is mirror symmetric about $Z = 0$, the summation in E_{K_2} vanishes. Therefore, E_{K_2} will distort the cycloid to produce an energy reduction of order $-(K_2)^2/|J_1|$. Since $E_{K_2}/E_{K_3} \sim l^2 \ll 1$, E_{K_2} can be neglected as a source of three-fold symmetry breaking compared to E_{K_3} .

IV. MAGNETIC FIELDS

In this section and the next, we neglect the effects of domain pinning. The behavior of the domain wavevectors in an external field is then completely determined by the model developed above. The effects of pinning will be examined in Section V.

For $K_3 > 0$, E_{K_3} favors spins that lie along one of the three three-fold axis $\phi_i = 0$ and $\pm 2\pi/3$. With this additional anisotropy, the wavevectors \mathbf{q}_k rotate away from the three-fold axis with increasing field when the field does not itself lie perpendicular to a three-fold axis.

A. Field along a three-fold axis or $\mathbf{m} = \mathbf{X}$

First take the field along a three-fold axis such as \mathbf{X} in Fig.1. Assuming that the system has been cooled from high temperature in zero field, all three domains with wavevectors \mathbf{q}_k will be equally occupied. But in large field, we expect that the stable domain will have wavevector \mathbf{q}' parallel to \mathbf{Y} and perpendicular to \mathbf{m} . For $K_3 = 10^{-6}$ meV, the energy $E = \langle \mathcal{H} \rangle$ is evaluated for several different wavevectors at each field. Defining E_0 as the energy for $K_3 = 0$ and $B = 0$, results for $\Delta E = E - E_0$ are presented in Fig.2.

At zero field, ΔE is minimized when \mathbf{x}' lies along a three-fold axis. Since $\mathbf{m} = \mathbf{X}$ is itself a three-fold axis, minima appear when $|\mathbf{m} \cdot \mathbf{x}'| = 1$ or $1/2$. With increasing field, the minimum at $|\mathbf{m} \cdot \mathbf{x}'| = 1$ ($\mathbf{x}' \parallel \mathbf{m}$) increases in energy so that this solution is only metastable. The stable solutions rotate from $|\mathbf{m} \cdot \mathbf{x}'| = 1/2$ towards 0.

In addition to the critical field marking the transition into the CAF phase, we identify two lower critical fields. Below $B_{c1} \approx 4.6$ T, the minima at $|\mathbf{m} \cdot \mathbf{x}'| = 1$ survives so that the domain with wavevector along \mathbf{m} remains metastable. Above B_{c1} , that metastable domain disappears. As the field increases, the wavevectors of the stable domains rotate towards the orientation $\mathbf{Y} \perp \mathbf{m}$. In the absence of domain pinning, that rotation is complete at $B_{c2} \approx 5.5$ T.

For each field, the dependence of energy on $\mathbf{m} \cdot \mathbf{x}'$ can be described by a sixth order polynomial with even terms only. Based on the polynomial fits given by the solid curves in Fig.2, we obtain the minimum energy solutions for $|\mathbf{m} \cdot \mathbf{x}'|$ at each field. We plot $|\mathbf{m} \cdot \mathbf{x}'|_{\min}$ versus field in Fig.3. Above $B_{c2} \approx 5.5$ T, \mathbf{q} lies perpendicular to \mathbf{m} and $|\mathbf{m} \cdot \mathbf{x}'|_{\min} = 0$.

The critical fields are plotted against the three-fold anisotropy K_3 [33] in Fig.4(a). Both critical fields B_{c1} and B_{c2} and their difference $B_{c2} - B_{c1}$ increase quite rapidly $\sim \sqrt{K_3}$ for small K_3 . We schematically sketch the dependence of the satellite peaks on magnetic field and their energies in the insets to Fig.4.

B. Field perpendicular to a three-fold axis or $\mathbf{m} = \mathbf{Y}$

When the field lies along \mathbf{Y} , the orientation of the stable domain does not change with field, i.e. domain 2 with $\mathbf{x}' = [1, 0, -1] \perp \mathbf{m}$ or $\mathbf{m} \cdot \mathbf{x}' = 0$ is always stable. But as seen in Fig.5, domains 1 and 3 with $\mathbf{x}' = [0, 1, -1]$ and $[1, -1, 0]$ or $|\mathbf{m} \cdot \mathbf{x}'| = \sqrt{3}/2$ are metastable for small fields and become unstable at high fields.

As in the previous subsection, $\Delta E/N$ can be fit by a sixth order polynomial in $\mathbf{m} \cdot \mathbf{x}'$ (even terms only). When $K_3 = 10^{-6}$ meV, domains 1 and 3 are metastable below $B_{c1} \approx 3.1$ T. With increasing field, the orientations \mathbf{x}' of the metastable domains rotate slightly towards the three-fold axis perpendicular to \mathbf{m} , as seen in the top curve of Fig.3. At B_{c1} , $|\mathbf{m} \cdot \mathbf{x}'| = \sqrt{2}/2$ so that the domain

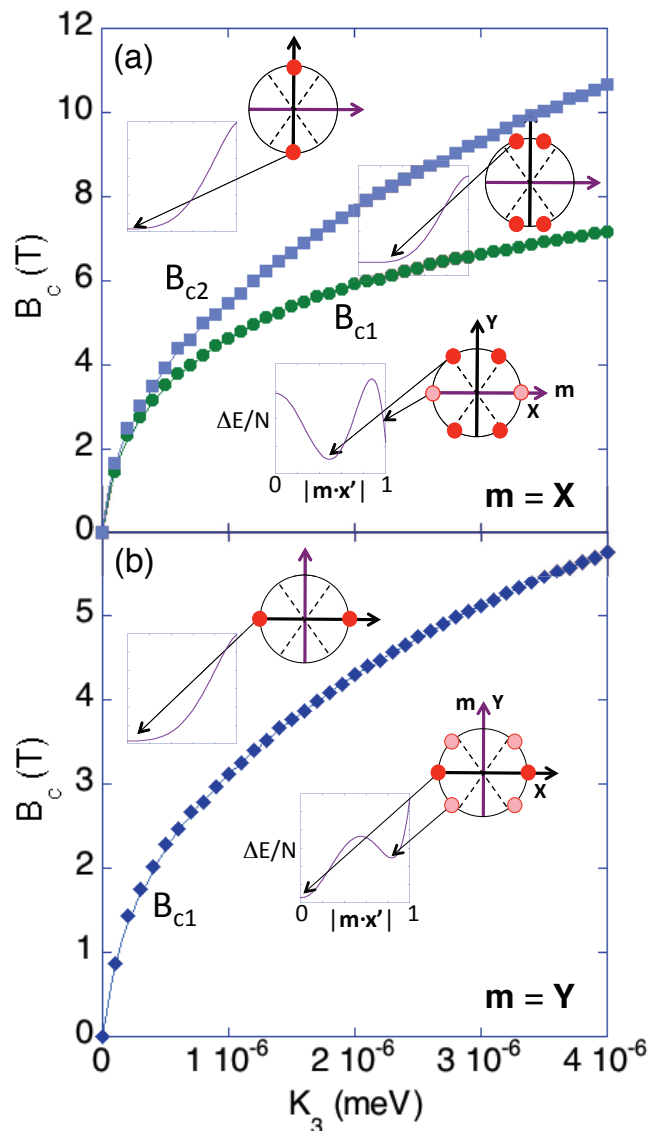


FIG. 4: (Color online) (a) The critical fields B_{c1} and B_{c2} versus three-fold anisotropy K_3 for $\mathbf{m} = \mathbf{X}$. (b) The critical field B_{c1} versus K_3 for $\mathbf{m} = \mathbf{Y}$. Insets schematically show the dependence of the satellites on field and their energies.

wavevectors \mathbf{q} have rotated from $\theta = \pm\pi/6$ away from \mathbf{Y} at zero field to $\pm\pi/4$ away from \mathbf{Y} at B_{c1} (although pinning will change this conclusion). Because the wavevector for domain 2 is already perpendicular to \mathbf{m} at zero field, $B_{c2} = 0$.

The dependence of B_{c1} on K_3 is shown in Fig.4(b) [33]. Once again, B_{c1} scales like $\sqrt{K_3}$ for small K_3 .

V. PINNING

The effects of pinning are essential to understand the behavior of the cycloidal domains in a magnetic field. Evidence for pinning was provided by recent SANS mea-

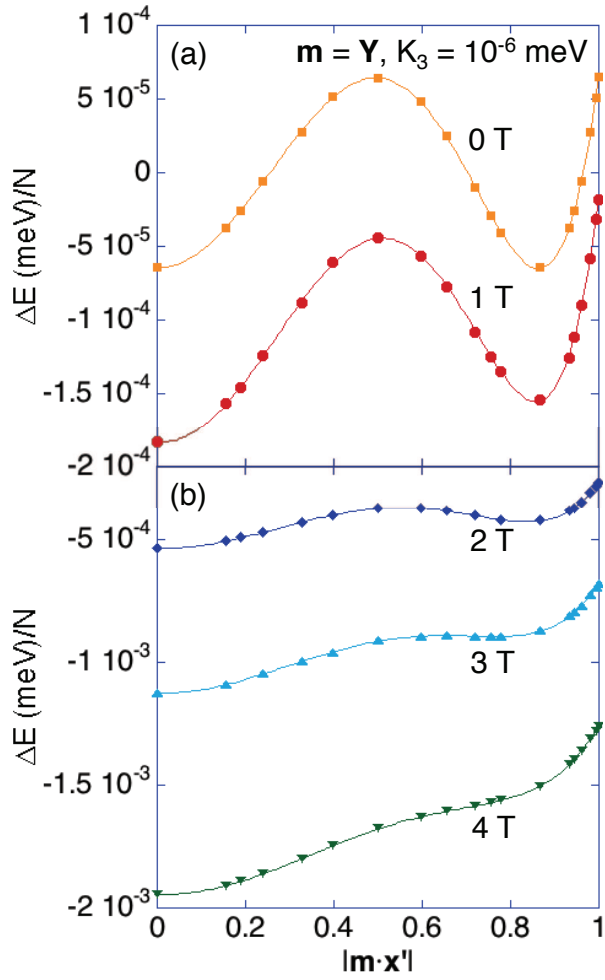


FIG. 5: (Color online) The energy $\Delta E/N$ versus wavevector $|\mathbf{m} \cdot \mathbf{x}'|$ for $K_3 = 10^{-6} \text{ meV}$ and field ranging from 0 to 4 T along \mathbf{Y} . Solid curves are fits to a sixth order polynomial in $\mathbf{m} \cdot \mathbf{x}'$.

surements [25]. For $\mathbf{m} = \mathbf{X}$, the wavevectors of the stable $\mathbf{x}' = [1, -1, 0]$ and $[0, -1, 1]$ domains remain unchanged up to about 5.5 T, above which they rotate towards $\mathbf{Y} \perp \mathbf{m}$. For $\mathbf{m} = \mathbf{Y}$, the wavevectors of the metastable $\mathbf{x}' = [1, -1, 0]$ and $[0, -1, 1]$ domains rotate towards $\mathbf{X} \perp \mathbf{m}$ above about 5 T.

In a ferromagnet, domain pinning is caused by structural defects that locally change the exchange interactions and anisotropies, creating a complex energy landscape with barriers between different orientations of the magnetization $\mathbf{M} = 2\mu_B \langle \mathbf{S}_i \rangle$ [34]. No doubt, these effects are also important in cycloidal spin systems. But the charge redistribution determined by the cycloidal wavevector \mathbf{q} may be even more important. Due to the strong magnetoelastic coupling in BiFeO_3 [35,36], this charge redistribution is pinned by non-magnetic impurities. Although the total magnetoelastic energy is independent of \mathbf{q} (see Appendix A), the distortions ϵ_{xx} , ϵ_{yy} , and ϵ_{zz} of the rhombohedral structure separately depend

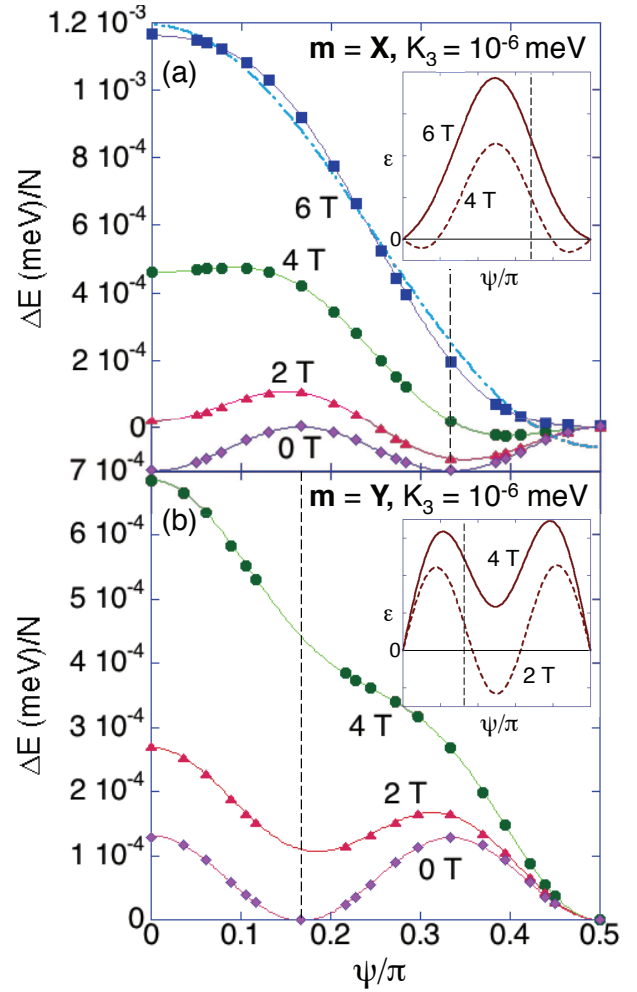


FIG. 6: (Color online) The energy $\Delta E/N$ versus angle $\psi = \cos^{-1}(\mathbf{m} \cdot \mathbf{x}')$ with ΔE set to zero at $\mathbf{m} \cdot \mathbf{x}' = 0$ or $\psi = \pi/2$ for (a) $\mathbf{m} = \mathbf{X}$ and (b) $\mathbf{m} = \mathbf{Y}$, both with $K_3 = 10^{-6} \text{ meV}$. Dashed vertical lines are at $\psi = \pi/3$ and $\pi/6$, respectively. Insets plot the derivative ϵ versus ψ . The dash-dot curve in (a) is a fit of the energy $\Delta E/N$ to second order in $\mathbf{m} \cdot \mathbf{x}' = \cos \psi$.

on the wavevector orientation. In order to rotate \mathbf{q} , the magnetic field must drag this lattice distortion, pinned by non-magnetic impurities, through the crystal. Of course, this charge redistribution is absent in a collinear AF.

The susceptibility χ_{\perp} for $\mathbf{B} \parallel \mathbf{y}'$ or perpendicular to the plane of the cycloid is much larger than the susceptibility χ_{\parallel} for \mathbf{B} within the cycloidal plane [19]. So the induced magnetization is $\mathbf{M} = \chi_{\perp} \mathbf{B}_{\perp}$ where \mathbf{B}_{\perp} is the component of \mathbf{B} along \mathbf{y}' . The external field $\mathbf{B} = \mathbf{B}_{\perp} + \mathbf{B}_{\parallel}$ plays two roles: \mathbf{B}_{\perp} produces the perpendicular magnetization \mathbf{M} and \mathbf{B}_{\parallel} exerts a torque $\boldsymbol{\tau} = \mathbf{M} \times \mathbf{B}$ on \mathbf{M} .

A. Microscopic model

To connect these considerations with our microscopic model, Fig.6 replots $\Delta E/N$ versus $\psi = \cos^{-1}(\mathbf{m} \cdot \mathbf{x}')$ while setting $\Delta E/N = 0$ at $\mathbf{m} \cdot \mathbf{x}' = 0$ or $\psi = \pi/2$. Using the angle definitions in Fig.7, note that $\psi = \theta$ for $\mathbf{m} = \mathbf{X}$ and $\psi = \phi = \pi/2 - \theta$ for $\mathbf{m} = \mathbf{Y}$. We propose that a domain is pinned until the downward slope $\varepsilon = -d(\Delta E/N)/d\psi$ exceeds the threshold $\varepsilon_{\text{pin}} > 0$. For $\mathbf{m} = \mathbf{X}$, ε decreases with ψ in the neighborhood of $\psi = \pi/3$, as seen in the inset to Fig.6(a). As ψ increases, larger fields are required to fulfill the condition $\varepsilon > \varepsilon_{\text{pin}}$. A similar result is found for $\mathbf{m} = \mathbf{Y}$ near $\psi = \pi/6$, as seen in Fig.6(b). In both cases, ψ satisfies the depinning condition $\varepsilon = \varepsilon_{\text{pin}}$ as the field increases.

In the limit of strong pinning, the condition $\varepsilon = \varepsilon_{\text{pin}}$ can be solved exactly. For large fields, the anisotropy can be ignored and $\Delta E/N = -MB \sin \psi$. To linear order in the field, $M = \chi_{\perp} B \sin \psi$ so that $\Delta E/N = -\chi_{\perp} B^2 \sin^2 \psi$ and $\varepsilon = \chi_{\perp} B^2 \sin 2\psi$.

For $\mathbf{m} = \mathbf{X}$, the energy $\Delta E/N$ is fairly well-described by the form given above $\propto \sin^2 \psi$ at high fields, as seen by the dash-dot curve in Fig.6(a) for 6 T. This agreement improves with increasing field. Consequently, $\varepsilon \propto \sin 2\psi$ is close to the form in the inset to Fig.6(a) near $\psi = \theta = \pi/3$ or $\phi = \pi/6$. So for strong pinning, ϕ satisfies the condition

$$\sin 2\phi = \frac{\sqrt{3}}{2} \left(\frac{B_{\text{pin}}}{B} \right)^2, \quad (19)$$

where the pinning field $B_{\text{pin}}^2 = 2\varepsilon_{\text{pin}}/\sqrt{3}\chi_{\perp}$ is defined so that $\phi = \pi/6$ when $B = B_{\text{pin}}$.

For $\mathbf{m} = \mathbf{Y}$, the expression $\varepsilon \propto \sin 2\psi$ is not satisfied until fields far above B_{c1} . So the simplified expression of Eq.(19) cannot be applied when $\mathbf{m} = \mathbf{Y}$ and $\psi = \phi = \pi/6$. Hence, the depinning condition $\varepsilon = \varepsilon_{\text{pin}}$ must be solved numerically.

Nonetheless, we can still draw some qualitative conclusions. The inset to Fig.6(b) indicates that domains 1 and 3 become unstable when $\varepsilon > 0$ for $\psi = \phi = \pi/4$. So in the absence of pinning, ψ will grow from $\pi/6$ in zero field to $\pi/4$ at B_{c1} , in agreement with Fig.3. Taking pinning into account, there are two possible ways for domains 1 and 3 to evolve with field. If $B_{\text{pin}} > B_{c1}$, then the domains will disappear only after becoming depinned at B_{pin} with $\psi = \pi/6$. If $B_{\text{pin}} < B_{c1}$, then ψ will start rotating from $\pi/6$ towards $\pi/4$ above B_{pin} and stop rotating at B_{c1} with $\psi < \pi/4$. So the rotation towards $\pi/4$ is not completed.

B. Landau-Lifshitz-Gilbert equation

Another way to approach pinning is through the Landau-Lifshitz-Gilbert (LLG) equation [37] for the time dependence of the magnetization:

$$\frac{\partial \mathbf{M}}{\partial t} = -2\mu_B \boldsymbol{\tau} + \gamma \mathbf{M} \times \boldsymbol{\tau}, \quad (20)$$

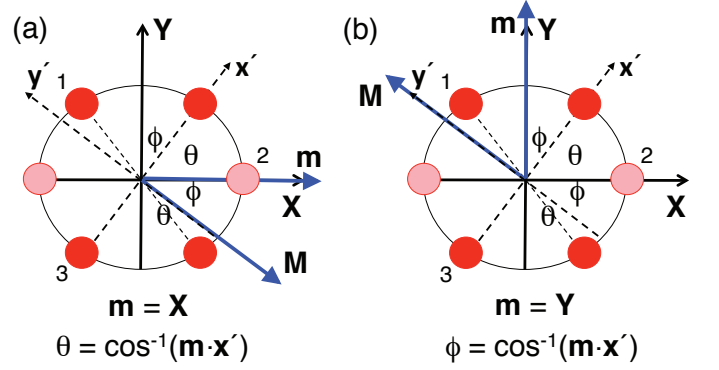


FIG. 7: (Color online) The magnetization and the cycloidal \mathbf{x}' and \mathbf{y}' axis for domain 3 with (a) $\mathbf{m} = \mathbf{X}$ and (b) $\mathbf{m} = \mathbf{Y}$. Also shown are angles θ and $\phi = \pi/2 - \theta$.

where $\boldsymbol{\tau} = \mathbf{M} \times \mathbf{B}_{\text{eff}}$ is the torque and \mathbf{B}_{eff} is an effective field that includes the effect of anisotropy. The first term in the LLG equation produces the precession of \mathbf{M} about \mathbf{B}_{eff} and the second term gives the damping of \mathbf{M} as it approaches equilibrium. So γ is proportional to the inverse of the relaxation time of the spins.

In the strong-pinning limit (see the discussion at the end of this section), we can neglect anisotropy and set $\mathbf{B}_{\text{eff}} = \mathbf{B}$. Since \mathbf{M} rotates within the $\mathbf{X} - \mathbf{Y}$ plane, it can be written $\mathbf{M} = M(\cos \varphi \mathbf{X} + \sin \varphi \mathbf{Y})$ so that

$$\boldsymbol{\tau} = \mathbf{M} \times \mathbf{B} = M \left\{ B_Z (\sin \varphi \mathbf{X} - \cos \varphi \mathbf{Y}) + (B_Y \cos \varphi - B_X \sin \varphi) \mathbf{Z} \right\}. \quad (21)$$

The LLG equation then gives

$$\begin{aligned} \frac{d\varphi}{dt} &= -2\mu_B B_Z - \gamma M (B_Y \cos \varphi - B_X \sin \varphi) \\ &= -2\mu_B B_Z - \gamma \tau_Z. \end{aligned} \quad (22)$$

When $\mathbf{m} = \mathbf{X}$, $\varphi = -\phi$ and $M = \chi_{\perp} B \cos \phi$ so

$$\tau_Z = \frac{\chi_{\perp} B^2}{2} \sin 2\phi = \frac{\varepsilon}{2}. \quad (23)$$

Hence, the torque along \mathbf{Z} and the energy derivative ε are simply related in the strong-pinning limit. Ignoring the precession of \mathbf{M} about \mathbf{Z} induced by B_Z , the relaxation of ϕ towards equilibrium within the $\mathbf{X} - \mathbf{Y}$ plane is determined by $\tau_Z = \varepsilon/2$.

Pinning in a ferromagnet is described by an effective field [26,27] that opposes the applied field, both along \mathbf{M} . In the strong-pinning limit of a cycloidal spin system, the external torque $\boldsymbol{\tau}$ along \mathbf{Z} is opposed by a pinning torque with maximum magnitude τ_{pin} . The conditions $\tau_Z = \tau_{\text{pin}}$ and $\varepsilon = \varepsilon_{\text{pin}}$ are then equivalent. In terms of τ_{pin} , the pinning field is given by $B_{\text{pin}}^2 = 4\tau_{\text{pin}}/\sqrt{3}\chi_{\perp}$.

For $\mathbf{m} = \mathbf{X}$, Eq.(19) is solved for ϕ as a function of B/B_{pin} in Fig.8. As shown in the next section, Eq.(19)

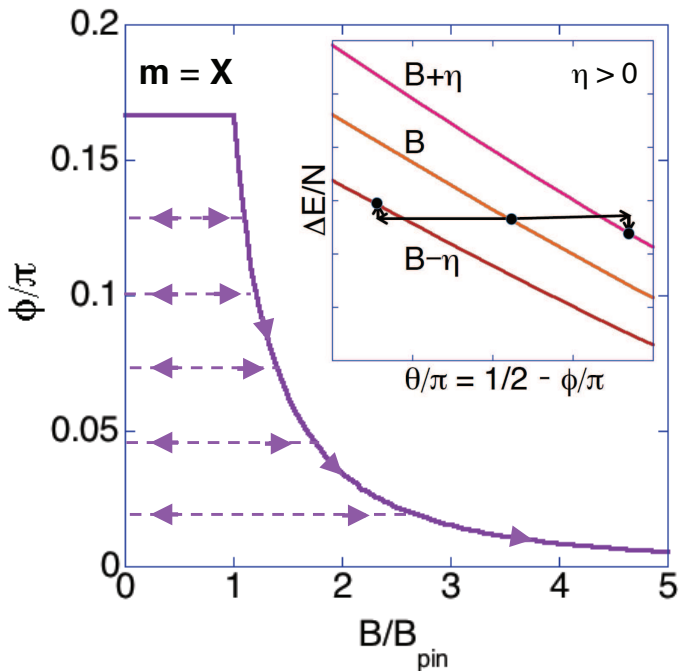


FIG. 8: (Color online) With $\mathbf{m} = \mathbf{X}$, the evolution of the rotation angle ϕ for domains 1 and 3 with field B normalized by B_{pin} . The solid curve is for increasing field, the dashed lines are for decreasing or increasing field. Inset shows that $\Delta E/N$ would have to rise with decreasing field to keep its downward slope ε unchanged. For increasing field, $\Delta E/N$ drops.

can be refined by expanding χ_{\perp} in powers of $B^2 \cos^2 \phi$. Since ϕ never reaches 0, $B_{c2} = \infty$.

Because the charge redistribution evaluated in Appendix A only depends on the direction of \mathbf{q} , τ_Z does not depend on the interior details of the cycloid such as its period or higher harmonics, but only on the magnetization \mathbf{M} induced by \mathbf{B}_{\perp} .

For $\mathbf{m} = \mathbf{X}$, experiments [25] observe pinning when B is lowered from B_{pin} but not as it is raised. This can be easily explained based on our model. For a fixed slope $\varepsilon = \varepsilon_{\text{pin}}$, $\Delta E/N \propto \cos^2 \theta / \sin 2\theta$ decreases with increasing $\theta \geq \pi/3$, as shown in the inset to Fig.8. So when B is raised from B_{pin} , $\phi = \pi/2 - \theta$ relaxes to a smaller value with lower energy. But when B is lowered from B_{pin} , ϕ would have to take a larger value with *higher* energy to satisfy the condition $\varepsilon = \varepsilon_{\text{pin}}$ or $\tau_Z = \tau_{\text{pin}}$. This process is energetically prohibited at low temperatures. The pinning of domains with decreasing field is shown by the dashed lines in Fig.8. When the field is ramped up again with this value of ϕ , \mathbf{q} will only start rotating towards smaller values of ϕ when the condition given by Eq.(19) is reached at the solid curve.

VI. RESULTS

Let's use these ideas to examine the experimental results for BiFeO₃. We separately discuss the two cases for field along \mathbf{X} or \mathbf{Y} examined in Section IV.

First take $\mathbf{m} = \mathbf{X}$ as in Section IV.A. Since domain 2 with $\mathbf{q}_2 \parallel \mathbf{m}$ becomes unstable when $B > B_{c1} \approx 7$ T [25], the dependence of B_{c1} on K_3 from Fig.4 implies that $K_3 \approx 3.65 \times 10^{-6}$ meV. The pinning field $B_{\text{pin}} \approx 5.6$ T for domains 1 and 3 is estimated from experimental results. Measurements by Bordacs *et al.* [25] confirm that the wavevectors of domains 1 and 3 never become fully perpendicular to $\mathbf{m} = \mathbf{X}$ but that $\phi \rightarrow 0$ or $\theta \rightarrow \pi/2$ with increasing field.

This model can be further refined by expanding χ_{\perp} in powers of $B^2 \cos^2 \phi$. With $b = B/B_{\text{pin}}$,

$$\chi_{\perp}(b) = \chi_0 + \chi_2 b^2 \cos^2 \phi, \quad (24)$$

where χ_2 is the non-linear susceptibility. Defining $\alpha = \chi_2/\chi_0$, we numerically solve

$$b^2 \left\{ 1 + \alpha b^2 \cos^2 \phi \right\} \sin 2\phi = \frac{\sqrt{3}}{8} (4 + 3\alpha) \quad (25)$$

with pinning field

$$B_{\text{pin}}^2 = \frac{4}{\sqrt{3}} \frac{\tau_{\text{pin}}}{\chi_0 + 3\chi_2/4}. \quad (26)$$

The solutions to Eq.(25) with $\alpha = 0.2$ and 0.4 are plotted in the dashed curves of Fig.9 and are in good agreement with measurements. As mentioned above, the dependence of ϕ on field given by Eq.(25) may only be approached at large fields if the condition for the strong-pinning limit is not met at B_{pin} .

Now take $\mathbf{m} = \mathbf{Y}$ as in Section IV.B. Then domain 2 with $\mathbf{q}_2 \perp \mathbf{m}$ is always stable. Unfortunately, the rotation of domains 1 and 3 cannot be treated in the strong-pinning limit. In particular, B_{pin} may differ from the earlier result for $\mathbf{m} = \mathbf{X}$. Experiments with $\mathbf{m} = \mathbf{Y}$ indicate that domains 1 and 3 rotate by about 9 degrees before disappearing between 6 and 7 T. This implies that the second scenario discussed above with $B_{c1} > B_{\text{pin}}$ is applicable. As expected, $\psi = \phi$ has only increased to about $39^\circ < 45^\circ$ at B_{c1} . But for $K_3 = 3.65 \times 10^{-6}$ meV, Fig.4(b) predicts that $B_{c1} \approx 5.6$ T, which is below the range of observed values where the domains disappear. This discrepancy can possibly be explained by a slight misalignment of the field out of the $\mathbf{X} - \mathbf{Y}$ plane.

Since τ_{pin} depends on the concentration and distribution of non-magnetic impurities, it may also change in different samples. Because the samples used in the spectroscopy [16] and SANS measurements [25] come from different sources, their pinning torques may be different as well. Based on the relative purities of these two samples, B_{pin} may be larger than indicated above for the sample used in the spectroscopy measurements. The observed spread [25] in wavevectors \mathbf{q}_1 and \mathbf{q}_3 near \mathbf{Y}

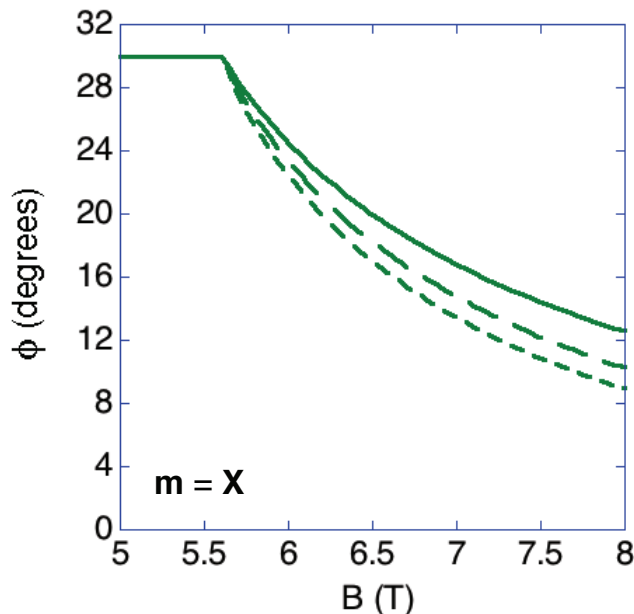


FIG. 9: (Color online) Model predictions for $B_{\text{pin}} = 5.6$ T and $\alpha = 0$ (solid), 0.2 (long dash), or 0.4 (short dash).

for $\mathbf{m} = \mathbf{X}$ also suggests that the pinning torque τ_{pin} varies from one domain to another throughout the sample used in the SANS measurements. Unlike τ_{pin} , B_{c1} is determined by the relative energies of different domain wavevectors \mathbf{q} and is independent of sample quality.

The “strong-pinning” limit is reached when the anisotropy K_3 makes a negligible contribution to the energy compared to the pinning field B_{pin} . Considering the contributions of the magnetic field and the anisotropy to the energy, the strong-pinning limit requires that $B_{\text{pin}}M \gg 2S^6K_3$ or

$$B_{\text{pin}}^2 \gg \frac{2S^6K_3}{\chi_{\perp}}. \quad (27)$$

Using the definition of B_{pin} in terms of the pinning torque τ_{pin} , the strong-pinning limit requires that $\tau_{\text{pin}} \gg \sqrt{3}S^6K_3/2$. Taking $K_3 = 3.65 \times 10^{-6}$ meV and χ_{\perp} from measurements [3], these conditions require that $B_{\text{pin}} \gg 2.5$ T and $\tau_{\text{pin}} \gg 0.77$ μeV .

Even for small B_{pin} , the strong-pinning limit can be reached when the field is sufficiently large that it dominates the energy. This condition is given by Eq.(27) with B replacing B_{pin} . So independent of B_{pin} , Eq.(19) for the dependence of ϕ on field is approached when $B \gg 2.5$ T.

VII. DISCUSSION

This work resolves all of the discrepancies with earlier measurements listed in the introduction. Not too close to the poles at $\pm\mathbf{z}'$, the critical field $B_{c3} > 16$ T above which the CAF phase becomes stable does not sensitively depend on the azimuthal angle ζ because \mathbf{q} is then nearly perpendicular to \mathbf{m} . This explains the earlier discrepancy with measurements by Tokunaga *et al.* [23]. For any ζ , Ref.[22] then predicts that B_{c3} will increase monotonically as the polar angle ϑ decreases from $\pi/2$ at the equator to zero at the poles.

Because it couples to the wavevector orientation but not to the individual spins, the strain does not directly affect the spin dynamics. However, it may be necessary to slightly raise K_1 to compensate for the effect of K_3 , which favors the spins lying in the $\mathbf{X} - \mathbf{Y}$ plane [38]. Since the total magnetoelastic energy is independent of \mathbf{q} , it does not alter the relative energies of different wavevectors in Figs.2 and 5. Measurements of the lattice strain in a magnetic field along a three-fold axis like \mathbf{X} can test this hypothesis.

How does our estimate for K_3 in BiFeO_3 compare with that in other materials? The constant K_3 can be estimated from the angular dependence of the basal-plane magnetization or the torque. For Co_2Y ($\text{Y} = \text{Ba}_2\text{Fe}_{12}\text{O}_{22}$) and Co_2Z ($\text{Z} = \text{Ba}_3\text{Fe}_{24}\text{O}_{41}$), $\tilde{K}_3 \equiv S^6K_3/V_c \approx 600$ erg/cm³ and 1500 erg/cm³, respectively [39] (V_c is the volume for one magnetic ion). For pure Co, $\tilde{K}_3 \approx 1.2 \times 10^5$ erg/cm³ [40]. Anisotropy energies are much larger for the rare earths than for transition-metal oxides [41]. While $\tilde{K}_3 \approx 6300$ erg/cm³ for Gd, it is about 1000 times higher for the heavier rare earths Tb, Dy, Ho, Er, and Tm. By comparison, $K_3 = 3.65 \times 10^{-6}$ meV for BiFeO_3 corresponds to $\tilde{K}_3 = 2.4 \times 10^4$ erg/cm³, about 4 times larger than for Gd but smaller than for pure Co.

Our discussion of domain pinning was motivated by previous results for ferromagnets. For a ferromagnet, thermally activated creep [42] allows the domain walls to move even when $B < B_{\text{pin}}$. It seems likely that a similar effect in BiFeO_3 allows the domains to rotate at nonzero temperature even when $\tau_Z < \tau_{\text{pin}}$ or $\varepsilon < \varepsilon_{\text{pin}}$.

We conclude that the “canonical” model of BiFeO_3 must be augmented by three-fold anisotropy and magnetoelastic energies in order to explain the field evolution of a domain when \mathbf{q} is not perpendicular to \mathbf{m} . Over the past decade, our understanding of BiFeO_3 has greatly increased but so have the number of new mysteries to be solved. At least at low temperatures, we believe that the modified Hamiltonian presented in this work can be used to study the manipulation of domains by magnetic and electric fields.

Thanks to Sandor Bordács, Takeshi Egami, Daniel Farkas, and Istvan Kézsmárki for helpful discussions. Research sponsored by the U.S. Department of Energy, Office of Basic Energy Sciences, Materials Sciences and Engineering Division.

Appendix A: Magnetoelastic Coupling

This appendix describes the effects of the magnetoelastic coupling in BiFeO₃. The magnetoelastic energy is given by

$$\begin{aligned} \frac{1}{V}H_{me} = & \frac{1}{2}c_{11}(\epsilon_{xx}^2 + \epsilon_{yy}^2 + \epsilon_{zz}^2) \\ & + c_{12}(\epsilon_{xx}\epsilon_{yy} + \epsilon_{yy}\epsilon_{zz} + \epsilon_{zz}\epsilon_{xx}) \\ & + \frac{g}{N} \sum_i \left\{ \epsilon_{xx}S_{ix}^2 + \epsilon_{yy}S_{iy}^2 + \epsilon_{zz}S_{iz}^2 \right\}, \quad (\text{A1}) \end{aligned}$$

where c_{11} and c_{12} are the elastic coupling constants, g is the magnetoelastic coupling strength, and ϵ_{ii} are the strain components.

Minimizing this energy with respect to the strain components yields

$$\epsilon_{xx} = -\frac{g}{F} \left\{ (c_{11} + c_{12})M_{2x} - c_{12}(M_{2y} + M_{2z}) \right\}, \quad (\text{A2})$$

$$\epsilon_{yy} = -\frac{g}{F} \left\{ (c_{11} + c_{12})M_{2y} - c_{12}(M_{2x} + M_{2z}) \right\}, \quad (\text{A3})$$

$$\epsilon_{zz} = -\frac{g}{F} \left\{ (c_{11} + c_{12})M_{2z} - c_{12}(M_{2x} + M_{2y}) \right\}, \quad (\text{A4})$$

where

$$M_{2\alpha} = \frac{1}{N} \sum_i \langle S_{i\alpha}^2 \rangle \quad (\text{A5})$$

and $F = (c_{11} + 2c_{12})(c_{11} - c_{12})$. In terms of these variables, the magnetoelastic energy $E_{me} = \langle H_{me} \rangle$ is given by

$$\begin{aligned} \frac{1}{N}E_{me} = & -g^2 \frac{V}{2N} \frac{c_{11} + c_{12}}{F} \left\{ M_{2x}^2 + M_{2y}^2 + M_{2z}^2 \right\} \\ & + g^2 \frac{V}{N} \frac{c_{12}}{F} \left\{ M_{2x}M_{2y} + M_{2x}M_{2z} + M_{2y}M_{2z} \right\}, \quad (\text{A6}) \end{aligned}$$

where $V/N = a^3$.

Transforming $M_{2\alpha}$ into the local reference frame of the cycloid, we find

$$M_{2\alpha} = \frac{q_\alpha^2}{|\mathbf{q}|^2} M_{2x'} + \frac{1}{3} M_{2z'}, \quad (\text{A7})$$

which uses $M_{2y'} \approx 0$. For weak anisotropy, $M_{2x'} \approx M_{2z'} = S^2/2$ and

$$\frac{1}{N}E_{me} = -\frac{g^2 S^4 V}{4F} \frac{V}{N} (3c_{11} - 2c_{12}), \quad (\text{A8})$$

which is independent of \mathbf{q} .

However, the individual strain components

$$\epsilon_{\alpha\alpha} = -\frac{gS^2}{2F} \left\{ \frac{q_\alpha^2}{|\mathbf{q}|^2} (c_{11} + 2c_{12}) + \frac{1}{3} (c_{11} - 4c_{12}) \right\} \quad (\text{A9})$$

do depend on \mathbf{q} . In fact, roughly 75% of the strain depends on the wavevector orientation. Impurities clamp this lattice strain within the sample. Because the magnetic field must drag this distortion while rotating the cycloidal wavevector \mathbf{q} , impurities pin the orientation of the wavevector at low fields. Note that the volume change

$$\frac{\Delta V}{V} = \epsilon_{xx} + \epsilon_{yy} + \epsilon_{zz} = -\frac{gS^2}{c_{11} + 2c_{12}} \quad (\text{A10})$$

is independent of the wavevector orientation.

-
- ¹ W. Eerenstein, N. D. Mathur, and J. F. Scott, *Nature* (London) **442**, 759 (2006).
² T. Zhao, A. Scholl, F. Zavaliche, K. Lee, M. Barry, A. Doran, M.P. Cruz, Y.H. Chu, C. Ederer, N.A. Spaldin, R.R. Das, D.M. Kim, S.H. Baek, C.B. Eom, and R. Ramesh, *Nat. Mat.* **5**, 823 (2006).
³ M. Tokunaga, M. Akaki, T. Ito, S. Miyahara, A. Miyake, H. Kuwahara, and N. Furukawa, *Nat. Comm.* **6**, 587 (2015).
⁴ J.-G. Park, M.D. Lee, J. Jeong, and S. Lee, *J. Phys.: Cond. Mat.* **26**, 433202 (2014).
⁵ J.R. Teague, R. Gerson, and W.J. James, *Sol. St. Comm.* **8**, 1073 (1970).
⁶ D. Lebeugle, D. Colson, A. Forget, and M. Viret, *Appl. Phys. Lett.* **91**, 022907 (2007).
⁷ I. Sosnowska, T. Peterlin-Neumaier, and E. Steichele, *J. Phys. C: Solid State Phys.* **15**, 4835 (1982).
⁸ I. Sosnowska and A.K. Zvezdin, *J. Mag. Mag. Matter.* **140-**

- 144**, 167 (1995).
⁹ R. de Sousa and J.E. Moore, *Phys. Rev. B* **77**, 012406 (2008).
¹⁰ A. P. Pyatakov and A. K. Zvezdin, *Eur. Phys. J. B* **71**, 419 (2009).
¹¹ D. Rahmedov, D. Wang, J. Íñiguez, and L. Bellaiche, *Phys. Rev. Lett.* **109**, 037207 (2012).
¹² R.S. Fishman, J.T. Haraldsen, N. Furukawa, and S. Miyahara, *Phys. Rev. B* **87**, 134416 (2013).
¹³ R.S. Fishman, *Phys. Rev. B* **87**, 224419 (2013).
¹⁴ P. Rovillain, M. Cazayous, Y. Gallais, A. Sacuto, R.P.S.M. Lobo, D. Lebeugle, and D. Colson, *Phys. Rev. B* **79**, 180411(R) (2009).
¹⁵ D. Talbayev, S. A. Trugman, S. Lee, H. T. Yi, S.-W. Cheong, and A. J. Taylor, *Phys. Rev. B* **83**, 094403 (2011).
¹⁶ U. Nagel, R.S. Fishman, T. Katuwal, H. Engelkamp, D. Talbayev, H.T. Yi, S.-W. Cheong, and T. Rõöm, *Phys. Rev. Lett.* **110**, 257201 (2013).

- ¹⁷ This paper uses the parameters $J_1 = -5.3$ meV, $J_2 = -0.2$ meV, $K_1 = 0.004$ meV, $D_1 = 0.18$ meV, and $D_2 = 0.06$ meV, which reproduce the zero-field mode frequencies [12] scaled by $S = 5/2$ rather than by $\sqrt{S(S+1)} \approx 3$.
- ¹⁸ M. Ramazanoglu, M. Laver, W. Ratcliff II, S.M. Watson, W.C. Chen, A. Jackson, K. Kothapalli, S. Lee, S.-W. Cheong, and V. Kiryukhin, *Phys. Rev. Lett.* **107**, 207206 (2011).
- ¹⁹ D. Lebeugle, D. Colson, A. Forget, M. Viret, P. Bonville, J.F. Marucco, and S. Fusil, *Phys. Rev. B* **76**, 024116 (2007).
- ²⁰ D.G. Farkas, I. Kézsmárki, S. Bordács, T. Rõöm, U. Nagel, *et al.* (*unpublished*).
- ²¹ E. Matsubara, T. Mochpuchp, M. Nagai, and M. Ashida, *Phys. Rev. B* **94**, 054426 (2016).
- ²² R.S. Fishman, *Phys. Rev. B* **88**, 104419 (2013).
- ²³ M. Tokunaga, M. Azuma, and Y. Shimakawa, *J. Phys. Soc. Japan* **79**, 064713 (2010).
- ²⁴ J. Park, S.-H. Lee, S. Lee, F. Gozzo, H. Kimura, Y. Noda, Y.J. Choi, V. Kiryukhin, S.-W. Cheong, Y. Jo, E.S. Choi, L. Balicas, G.S. Jeon, and J.-G. Park, *J. Phys. Soc. Japan* **80**, 114714 (2011).
- ²⁵ S. Bordács, I. Kézsmárki, and D. Farkas, (*unpublished*).
- ²⁶ S. Lemerle, J. Ferré, C. Chappert, V. Mathet, T. Giamarchi, and P. Le Doussal, *Phys. Rev. Lett.* **80**, 849 (1998).
- ²⁷ W. Kleeman, J. Rhensius, O. Petravic, J. Ferré, J.P. Jamet, and H. Bernas, *Phys. Rev. Lett.* **99**, 097203 (2007).
- ²⁸ J.H. Lee, I. Kézsmárki, and R.S. Fishman, *New J. Physics* **18**, 040325 (2016).
- ²⁹ In the continuum limit $\lambda/a \rightarrow \infty$,
- $$\frac{\mathcal{H}_{D_1}}{N} \rightarrow \frac{D_1 a}{\lambda} \mathbf{y}' \cdot \int_0^{2\pi} d\rho \left(\mathbf{S}_\rho^{(1)} \times \frac{\partial \mathbf{S}_\rho^{(2)}}{\partial \rho} \right),$$
- $$\frac{\mathcal{H}_{D_2}}{N} \rightarrow \frac{3D_2}{2\pi} \mathbf{z}' \cdot \int_0^{2\pi} d\rho \left(\mathbf{S}_\rho^{(1)} \times \mathbf{S}_\rho^{(2)} \right),$$
- where $\rho = \mathbf{q} \cdot \mathbf{R}$.
- ³⁰ C. Weingart, N. Spaldin, and E. Bousquet, *Phys. Rev. B* **86**, 094413 (2012).
- ³¹ P. Bruno, *Phys. Rev. B* **39**, 865 (1989).
- ³² Higher-order easy-axis anisotropy terms $-S^4 \bar{K}_2 \sum_i \cos^4 \theta_i$ and $-S^6 \bar{K}_3 \sum_i \cos^6 \theta_i$ are also consistent with the $R3c$ crystal structure of BiFeO₃ but they do not produce any qualitatively new effects. Since the easy-axis $-S^2 K_1 \sum_i \cos^2 \theta_i$ term is already included in \mathcal{H} , we neglect those terms.
- ³³ To evaluate B_{c1} with $\mathbf{m} = \mathbf{X}$, we compare the energies of domains with wavevectors $[1, 0, -1]$ ($\mathbf{m} \cdot \mathbf{x}' = 1$) and $[5, 1, -6]$ ($\mathbf{m} \cdot \mathbf{x}' = 0.99$). Below B_{c1} , the domain with wavevector $[1, 0, -1]$ has lower energy; above B_{c1} , it has higher energy. To evaluate B_{c2} with $\mathbf{m} = \mathbf{X}$, we compare the energies of domains with wavevectors $[-1, 2, -1]$ ($\mathbf{m} \cdot \mathbf{x}' = 0$) and $[-2, 5, -3]$ ($\mathbf{m} \cdot \mathbf{x}' = 0.11$). Below B_{c2} , the domain with wavevector $[-2, 5, -3]$ has lower energy; above B_{c2} , it has higher energy. To evaluate B_{c1} with $\mathbf{m} = \mathbf{Y}$, we compare the energies of domains with wavevectors $[-4, 3, 1]$ ($\mathbf{m} \cdot \mathbf{x}' = 0.72$) and $[-3, 2, 1]$ ($\mathbf{m} \cdot \mathbf{x}' = 0.65$). Below B_{c1} , the domain with wavevector $[-4, 3, 1]$ has the lower energy; above B_{c1} , it has higher energy.
- ³⁴ T. Jourdan, F. Lançon, and A. Marty, *Phys. Rev. B* **75**, 094422 (2007)
- ³⁵ S. Lee, M.T. Fernandez-Diaz, H. Kimura, Y. Noda, D.T. Adroja, S. Lee, J. Park, V. Kiryukhin, S.-W. Cheong, M. Mostovoy, and J.-G. Park, *Phys. Rev. B* **88**, 060103(R) (2013).
- ³⁶ J.H. Lee and R.S. Fishman, *Phys. Rev. Lett.* **115**, 207203 (2016).
- ³⁷ L. Landau and L. Lifshitz, *Phys. Z. Sowjetunion* **8**, 153 (1935).
- ³⁸ The energy differences for a spin lying in the $\mathbf{X} - \mathbf{Y}$ plane and along \mathbf{z}' are $-K_1 S^2$ and $K_3 S^6$. So it may be necessary to raise K_1 by $\Delta K_1 = K_3 S^4$ to compensate for the effect of K_3 . For $K_3 = 3.65 \times 10^{-6}$ meV, this corresponds to a change $\Delta K_1 / K_1$ of about 3.5%.
- ³⁹ L.R. Bickford Jr., *Phys. Rev.* **119**, 1000 (1960).
- ⁴⁰ D.M. Paige, B. Szpunar, and B.K. Tanner, *J. Magn. Magn. Mat.* **44**, 239 (1984).
- ⁴¹ J. Rhyne, Ch.4 in *Magnetic Properties of Rare Earth Metals*, ed. R.J. Elliot (Plenum, London, 1972).
- ⁴² M.V. Feigel'man, V.B. Geshkenbein, A.I. Larkin, and V.M. Vinokur, *Phys. Rev. Lett.* **63**, 2303 (1989).